



## Research paper

## Impact of tropical cyclones on mooring designs of floating offshore wind turbines

Glib Ivanov<sup>a</sup> , Phuc-Manh-Dat Dang<sup>a</sup>, Wei-Ling Tsai<sup>a</sup>, Yuefan Du<sup>b</sup>, Ryota Wada<sup>b,\*</sup> , Kai-Tung Ma<sup>a,\*\*</sup>

<sup>a</sup> Department of Engineering Science and Ocean Engineering, National Taiwan University, Taipei, 106319, Taiwan

<sup>b</sup> Graduate School of Frontier Sciences, University of Tokyo, Tokyo, Japan

## ARTICLE INFO

## Keywords:

Wind  
Tropical cyclones  
Floating wind  
FOWT (floating offshore wind turbines)  
Mooring design

## ABSTRACT

Floating Offshore Wind Turbines (FOWTs) are emerging as a crucial and sustainable solution for effectively harnessing wind energy in deepwater regions. While winds are an essential source of sustainable energy, extreme environmental conditions imposed by tropical cyclones can be a challenge to the economics and feasibility of the FOWTs' mooring systems. This paper evaluates the impacts of environmental components (i.e., wind, waves, and currents) on mooring line tensions, particularly in regions with tropical cyclones, typhoons and hurricanes. Mooring analyses are performed on a semi-submersible FOWT with a 15 MW turbine for six different regions: Taiwan, Japan, Gulf of Mexico, West Australia, North Sea and West Africa. Based on the results of the mooring analysis, the impacts of 50-year events on mooring designs are assessed, and the differences among regions are compared. It was found that these tropical cyclone conditions can generate high tensions that may impact and influence the mooring designs, causing one of the regions, Taiwan, to adopt a 3x3 pattern with a maximum size of mooring chain. As a result, the cost of a floater's mooring system may be higher and potentially make FOWTs economically challenging. This paper closely assessed the intriguing phenomenon of the tension spikes caused partly by interactions among wind, waves, and currents. A general assessment of mooring loads for these regions is provided as a reference for future design work.

## 1. Introduction – mooring for floating wind turbines

There is a global trend toward the development of renewable energy sources, with offshore wind power emerging as one of the efficient solutions for sustainable energy generation. Reports from the GWEC (Lee et al., 2021) project that global offshore wind capacity will reach 10.9 GW by 2030. However, as suitable sites for fixed-bottom offshore wind turbines (OWTs) become increasingly scarce, floating offshore wind turbines (FOWTs) have gained prominence as a viable alternative (Ma et al., 2025).

Despite their significant potential, the development of offshore wind power in certain regions faces inherent challenges from tropical cyclones. The extreme wave heights and highly turbulent winds characteristic of these events can severely compromise the stability and structural resilience of floating wind turbine foundations, necessitating robust engineering considerations (Wada et al., 2025). These formidable hydrodynamic and aerodynamic forces demand particularly rigorous

structural design to ensure integrity.

The mooring system is a safety-critical component requiring meticulous design, especially when subjected to extreme environmental conditions. Its configuration, encompassing the number of lines, chain size, and length, is a primary design variable with a substantial impact on the overall cost of a floating offshore wind turbine (FOWT). The integrity of the mooring design is rigorously assessed under various design load conditions, including the Ultimate Limit State (ULS) and Fatigue Limit State (FLS). Previous research has indicated that ULS, rather than FLS, is the governing factor for mooring design in shallow water environments (Huang and Yang, 2021). Ivanov et al., 2024a, 2025 examined optimal mooring configurations for a semi-submersible FOWT in a typhoon environment. While a 3x2 mooring configuration is theoretically feasible, practical constraints related to the available chain size necessitate the adoption of a 3x3 mooring system for a region with typhoons. Li et al. (2024) analysed the influence of clump weights and heavy chains on reducing mooring tension during typhoons,

\* Corresponding author.

\*\* Corresponding author.

E-mail addresses: [r\\_wada@k.u-tokyo.ac.jp](mailto:r_wada@k.u-tokyo.ac.jp) (R. Wada), [kaitungma@ntu.edu.tw](mailto:kaitungma@ntu.edu.tw) (K.-T. Ma).

demonstrating that both methods effectively mitigate surge motion and tension fluctuations.

Consequently, the assessment of ULS conditions is of paramount importance for mooring design in tropical cyclone regions. ULS is typically defined by a 50-year return period, as stipulated by standards such as DNV (Grossmann-Matheson et al., 2024) and IEC (Bloemendaal et al., 2020a). Extensive research has explored statistical methodologies for defining design load cases for specific locations or datasets, often requiring extrapolation beyond observed periods, such as (Koohi et al., 2022; Sheng et al., 2020; Stanisic et al., 2018). Some studies emphasize joint extreme analysis, recognizing that independently estimating the 50-year return level for each environmental variable can yield overly conservative designs (Sando et al., 2024; Leong et al., 2018). Hang et al. (Xu et al., 2024) adopted a multi-spectrum approach to model wind and wave conditions, discretising the typhoon into different stages of its passage. The study highlighted that a single wind and wave spectrum is insufficient to fully capture the complex characteristics of a typhoon, particularly its turbulence, rapid fluctuations in wind speed, and sudden directional changes.

These studies have provided typical environmental conditions used for ULS assessment across major ocean basins. While numerous studies focus on FOWT mooring design for specific locations, a comparative analysis among different tropical cyclone-prone ocean basins remains notably absent. Various ocean basins are impacted by tropical cyclones, each possessing distinct climatological characteristics and formation mechanisms (Huang and Yang, 2021). The extreme environments within tropical cyclone regions are markedly different from those in non-cyclone regions, such as the North Sea (Ivanov et al., 2024a). We hypothesize that the varying environmental conditions across these different ocean basins, even within tropical cyclone regions, will lead to divergent optimal mooring configurations. This assumption stems from the premise that the impact of tropical cyclones is unique to each specific region, some with larger waves and some with stronger wind. It's generally intuitive that more severe weather conditions necessitate a greater number of mooring lines. However, the optimal mooring configuration becomes less clear when environmental variables exhibit disproportional strengths, such as strong winds coinciding with relatively smaller waves. Furthermore, the individual and combined contributions of wind, wave, and current to mooring tension, particularly under combined extreme conditions, have not been sufficiently explored to elucidate the underlying reasons for potential design differences.

The design of mooring systems for Floating Offshore Wind Turbines (FOWTs) in tropical cyclone-prone regions presents a significant challenge that must be overcome to enable the large-scale deployment of wind energy. A comprehensive understanding of the impact of tropical cyclones on mooring systems is crucial for enhancing existing design codes and ensuring structural resilience. This study presents the mooring configurations for a 15 MW semi-submersible FOWT across six distinct geographical regions: Taiwan, Japan, the Gulf of Mexico, West Australia, the North Sea, and West Africa. The primary objective is to elucidate the characteristics of mooring design in each region through comparative analysis. Furthermore, given the limited research directly quantifying the individual and combined effects of wind, waves, and particularly current on mooring tension, this investigation also aims to examine the contribution of each environmental factor to the total mooring tension under combined loading conditions.

The study employs an annual extreme value sampling method to select 50-year return period combined wind, wave, and current conditions for each location. Mooring analyses are subsequently performed using Design Load Case (DLC) 6.1, a standard specifically designed for ultimate limit state analysis under extreme environmental conditions. The resulting loads (tensions) on the mooring lines are thoroughly assessed, explicitly considering the complex interactions among wind, waves, and currents for both tropical cyclone-prone and non-tropical cyclone regions.

## 2. Numerical modelling on loads

The dynamic response of TaidaFloat under typhoon conditions was analysed through numerical simulations conducted using OrcaFlex, a fully coupled time-domain motion analysis software. OrcaFlex incorporates specialised modules for aerodynamics, hydrodynamics, and mooring dynamics, enabling a comprehensive simulation of the coupled response of the floating offshore wind turbine (FOWT). The governing equation of the dynamic response of a FOWT can be expressed using the Cummins equation (Cummins, 1962):

$$(M + A_\infty) \ddot{x}(t) + \int_0^t K(t-\tau) \dot{x}(\tau) d\tau + Gx(t) = F(t) \quad (1)$$

Where  $M$  represents the mass matrix,  $A_\infty$  is the fluid added mass matrix at infinite frequency,  $K(t)$  is the retardation function representing the fluid memory effects,  $G$  is the hydrostatic stiffness matrix of the semi-submersible,  $F(t)$  represents the external force including aerodynamic load, wave load, wind load, current load and mooring force. Substituting the forces at any instance can determine the platform acceleration ( $\ddot{x}(t)$ ) which can then be integrated to obtain the platform's new position. Next, the derivation of these forces is discussed.

### 2.1. Aerodynamic load on turbines

The aerodynamic loads acting on the wind turbine blades are computed using Blade Element Momentum theory (BEMT). Blade element theory assumes that each blade can be discretized into independent elements, each behaving aerodynamically as a two-dimensional aerofoil (Moriarty et al., 2005). The axial force ( $F_x$ ) and torque ( $T$ ) acting on one blade element is calculated as:

$$F_x = dL\cos\phi + dD\sin\phi = 0.5\rho W^2 c(C_L \cos \phi + C_D \sin \phi)dr \quad (2)$$

$$T = (dL\sin\phi - dD\cos\phi)r = 0.5\rho W^2 c(C_L \sin \phi - C_D \cos \phi)rdr \quad (3)$$

$$W = \sqrt{U_\infty^2(1-a)^2 + \Omega^2 r^2(1-a')^2} \quad (4)$$

Where  $C_L$  and  $C_D$  are the lift and drag coefficients of the sectional airfoil respectively,  $\rho$  is the air density,  $c$  is the chord length of the blade element. Parameters like  $r$ ,  $dr$ ,  $W$ ,  $c$ ,  $C_L$ ,  $C_D$ ,  $\phi$  varies among each blade element.  $\Omega$  is the rotor speed,  $W$  is the resultant relative velocity,  $r$  is the local radius of the blade element,  $U_\infty$  is the upstream velocity,  $a$  and  $a'$  are the axial and tangential induction coefficients, respectively.  $\alpha$ ,  $\beta$ ,  $\phi$  are angles of attack, twist, and inflow, respectively. The aerodynamic forces and torque on these elements are integrated along the blade span to determine the total forces and moments acting on the turbine.

### 2.2. Hydrodynamic load on platform

The hydrodynamic loads on the platform are evaluated using potential flow theory, which assumes the flow to be irrotational, inviscid, and incompressible. We follow the approach of previous research on hydrodynamic modules that do not include nonlinear waves nor breaking waves (Stanisic et al., 2017; Xu et al., 2021; Raillard et al., 2019). The velocity potential function is derived by solving the Laplace equation within the fluid domain while satisfying the free surface boundary conditions, seafloor surface boundary condition and body surface boundary condition (Barltrop, 1998).

The linearization decomposition of the velocity potential into:

$$\phi(x, y, z)e^{-iot} = \left[ \phi_I(x, y, z) + \phi_D(x, y, z) + \sum_{j=1}^6 x_j \phi_{r,j}(x, y, z) \right] e^{-iot} \quad (5)$$

$\phi_I$  is the potential of the incident wave,  $\phi_D$  is the diffraction wave potential and  $\phi_{r,j}$  is the radiation wave potential caused by the floating

body's unit motion amplitude.  $j$  represents the surge, sway, heave, roll, pitch, yaw motion of corresponding to 1 to 6 respectively.  $x_j$  is the motion amplitude in  $j$ -th direction.

Once the velocity potential is obtained, the pressure distribution on the body surface is determined using Bernoulli's equation:

$$p = -\rho(\phi_t + \nabla\phi \cdot \nabla\phi + gz) \quad (6)$$

On the right-hand side of Bernoulli's equation, three terms collectively define the total pressure. The first term represents the linear component of dynamic pressure. The second term corresponds to the quadratic pressure, which contributes to second-order forces. The third term denotes the hydrostatic pressure, which governs the restoring forces acting on the structure.

The first-order hydrodynamic loads acting on the floating platform are then computed by integrating the dynamic pressure over its wetted surface.

$$F_{EX}^{(1)} = \begin{cases} Re \left[ -\rho A e^{j\omega t} \iint_{S_b} n_i (\phi_I + \phi_D) dS \right] & (i = 1, 2, 3) \\ Re \left[ -\rho A e^{j\omega t} \iint_{S_b} (r^* n)_i (\phi_I + \phi_D) dS \right] & (i = 4, 5, 6) \end{cases} \quad (7)$$

With  $S_b$  and  $A$  are the wetted body surface and wave amplitude respectively.  $\omega$  is the frequency of the regular incident wave.

Beside the first order wave, the wave drift force, a second-order wave effect, is particularly significant for moored structures (Lee et al., 2005) and must be considered in the analysis. Using the momentum method, the mean forces can be expressed in terms of Kochin functions.

$$H(\theta) = \iint_{S_b} (\phi_{Bn} \phi_0 - \phi_B \phi_{0n}) dS \quad \phi_0 = Z(z) e^{-ivx \cos \beta - ivy \sin \beta} \quad (8)$$

And  $\phi_B$  is the total potential due to the body. The drift force is calculated as:

$$\left( \frac{F_x}{F_y} \right) = \frac{\rho v^3}{8\pi K} \frac{c_p}{2c_g} \int_0^{2\pi} |H(\theta)|^2 \begin{pmatrix} \cos \theta \\ \sin \theta \end{pmatrix} d\theta - \frac{\rho \omega A v}{2K} \begin{pmatrix} \cos \beta \\ \sin \beta \end{pmatrix} Im H'(\pi + \beta) \quad (9)$$

With  $c_p$  is the phase velocity,  $c_g$  is the group velocity,  $\beta$  is the angle between the direction of propagation of the incident wave and the positive x-axis.  $v$  is the wavenumber and is the positive real root of the dispersion relation  $K = vtanh(yh)$ .

### 2.3. Mooring load (tension)

The dynamic response of the mooring system is modelled using the lumped-mass approach (Cummins, 1962), where the mooring line is discretized into a series of  $N+1$  mass points, or nodes, connected by  $N$  massless elastic elements known as segments as shown in Fig. 1. Each

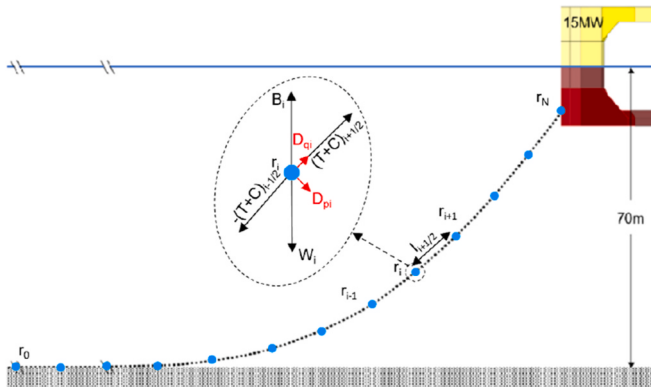


Fig. 1. Left: Lumped-mass model diagram.

segment represents a short portion of the mooring line and primarily captures its axial and torsional behaviour. Other physical properties, including mass, weight ( $W$ ), buoyancy, and hydrodynamic drag are concentrated at the nodes.

The equation of motion of each node  $i$  is:

$$\underbrace{[m_i + a_i]}_{\text{mass \& added mass}} \ddot{r}_i = T_{i+\left(\frac{1}{2}\right)} - T_{i-\left(\frac{1}{2}\right)} + C_{i+\left(\frac{1}{2}\right)} - C_{i-\left(\frac{1}{2}\right)} + \underbrace{W_i + B_i}_{\text{weight \& contact}} + \underbrace{D_{pi} + D_{qi}}_{\text{drag}} \quad (10)$$

In Equation (11) and Fig. 1,  $r_i[x_i, y_i, z_i]$  represents node  $i$ 's position and with that  $\ddot{r}_i$  is node  $i$ 's acceleration.  $T_{i+\left(\frac{1}{2}\right)}$  and  $C_{i+\left(\frac{1}{2}\right)}$  indicates the internal stiffness and damping forces in segment  $i+\left(\frac{1}{2}\right)$ . The weight  $W_i$  represents the lumped mass of node  $i$ .  $B_i$  indicates vertical reaction forces created by seabed interaction of node  $i$ .  $D_{pi}, D_{qi}$  represents transverse and tangential drag force respectively.

The lump-mass model employed in Orcaflex incorporate translational degrees of freedom, bend and torsional moments (Driscoll et al., 2000). shows that a one-dimensional lumped-mass model can also capture snap load. Compared to quasi-static method, lump-mass approach captures dynamic loads on the mooring line, including damping and inertia forces.

### 2.4. Wind and current load

The wind and current drag loads, resulting from the translational velocity of the air and water relative to the vessel, are computed in OrcaFlex using the standard OCIMF method (Haddara et al., 1999). The drag force corresponding to the relative velocity in the surge (or sway) direction is expressed as:

$$f_x = \frac{1}{2} C_{surge} \rho |v|^2 A_{surge} \quad f_y = \frac{1}{2} C_{sway} \rho |v|^2 A_{sway} \quad f_z = \frac{1}{2} C_{heave} \rho |v|^2 A_{heave} \quad (12)$$

$f_x, f_y, f_z$  are the drag force in the x-, y- and z-directions.  $C_{surge}, C_{sway}, C_{heave}$  are the current or wind drag coefficient in the x-, y- and z-directions respectively. These drag coefficients are calculated by CFD simulations, methodology details can be found in (Chen et al., 2023).  $\rho$  can be understood as water density for current force calculation and air density for wind force calculation.  $A_{surge}, A_{sway}, A_{heave}$  are the surge, sway and heave areas. For current these correspond to the exposed areas below the waterline, and for wind to the exposed areas above the waterline.  $v$  is the relative velocity of the sea or air past the vessel. In practice, the lateral and longitudinal movements of the platform will change the wind incident angle and the projected area, thereby feeding back and affecting the magnitude of the wind load. This effect is inherently included for lines (moorings and tower) in OrcaFlex, but not for the Floater due to software limitations. The floater is specifically designed to be stable, and the maximum pitch in Table 5 is only 7.3°, so its influence on the drag force is limited.

### 2.5. Wave-current interaction

An empirical formulation developed by Molin (Chen et al., 2023) from Aranha (1994) to account for the modification of wave drift forces due to the presence of a current. Let  $\vec{f}_d(\omega, \beta, 0, 0)$  denote the normalized drift force in a regular wave with frequency  $\omega$  and incidence  $\beta$ . Then with a current of velocity  $U_C$  and a direction  $\alpha$  superimposed, the new normalized drift force becomes:

$$\vec{f}_d(\omega, \beta, U_c, \alpha) = [1 + 4\tau \cos(\alpha - \beta)] \vec{f}_d(\omega[1 + \tau \cos(\alpha - \beta)], \beta + 2\tau \sin(\alpha - \beta), 0, 0) + O(\tau^2) \quad (13)$$

With  $\tau = U_c \omega / g$ , an interpretation of Equation (16) is that the current modifies the apparent wave amplitude, frequency, and direction, thereby altering the resulting drift force acting on the structure. We can rewrite Equation (16) as:

$$\vec{f}_d(\omega, \beta, U_c, \alpha) = \vec{f}_d(\omega, \beta, 0, 0) + \begin{pmatrix} b_{d11} & b_{d12} \\ b_{d21} & b_{d22} \end{pmatrix} \begin{pmatrix} U_c & \cos \alpha \\ U_c & \sin \alpha \end{pmatrix} + O(\tau^2) \quad (14)$$

With the components of the matrix  $b_d$  for infinite depth (for finite depth, see Malenica et al. (Malenica et al., 1995)) are given by:

$$b_{d11} = \left( \frac{4\omega}{g} f_{dx} + \frac{\omega^2}{g} \frac{\partial f_{dx}}{\partial \omega} \right) \cos \beta - \frac{2\omega}{g} \frac{\partial f_{dx}}{\partial \beta} \sin \beta \quad b_{d21} = \left( \frac{4\omega}{g} f_{dy} + \frac{\omega^2}{g} \frac{\partial f_{dy}}{\partial \omega} \right) \cos \beta - \frac{2\omega}{g} \frac{\partial f_{dy}}{\partial \beta} \sin \beta \quad (15)$$

$$b_{d12} = \left( \frac{4\omega}{g} f_{dx} + \frac{\omega^2}{g} \frac{\partial f_{dx}}{\partial \omega} \right) \sin \beta + \frac{2\omega}{g} \frac{\partial f_{dx}}{\partial \beta} \cos \beta \quad b_{d22} = \left( \frac{4\omega}{g} f_{dy} + \frac{\omega^2}{g} \frac{\partial f_{dy}}{\partial \omega} \right) \cos \beta + \frac{2\omega}{g} \frac{\partial f_{dy}}{\partial \beta} \cos \beta \quad (16)$$

These coefficients, referred to as wave drift damping, are implemented in OrcaFlex to represent wave-current interaction effects.

## 2.6. Extreme value extraction

For each simulated case there are 10 results as 10 random wave seeds are used, using statistic they can be converted to one value – the Most

Probable Maximum (MPM). The use of MPM is allowed by classification societies to avoid tension overestimation which leads to unnecessary expensive designs. In this study, we adopted the method introduced in DNVGL-OS-E301 (Hopstad et al., 2018) and summarized the steps in Fig. 2. This procedure is iteratively applied to each seed within a given environmental case. The resultant MPM value for the case is determined by averaging the MPM estimates obtained from 10 seeds (as suggested by DNV (Hopstad et al., 2018)).

## 3. Floating platform, mooring system and 15 MW wind Turbine

This study employs "TaidaFloat," a semi-submersible platform designed to support a 15 MW wind turbine (Ivanov et al., 2023; Hsu et al., 2022). The FOWT platform features a three-column configuration with flat panels and pontoons, specifically engineered for deployment in the Taiwan Strait off the coast of Hsinchu, which has received an approval-in-principle certificate from a class society, American Bureau of Shipping (ABS) (Wu et al., 2023), and was tank tested at a 1:100 scale (Lee et al., 2024; Haocheng et al., 2025). The design consists of a main column with a larger diameter that supports the wind turbine tower, complemented by two symmetrically arranged side columns of smaller diameter. Fig. 3 illustrates the floater's dimensions.

IEA 15 MW offshore wind turbine is used in this study (Gaertner et al., 2020) and will be placed on top of the main column of the floater as in (Ma et al., 2025). Table 1 shows the principal dimensions of the wind turbine.

The mooring system of TaidaFloat is a 3x3 catenary mooring system (Chen et al., 2023) with its properties shown in Table 1. According to (Ma et al., 2019), the horizontal stiffness due to the line's overall geometric deformation (assuming an inelastic mooring line) can be expressed as:

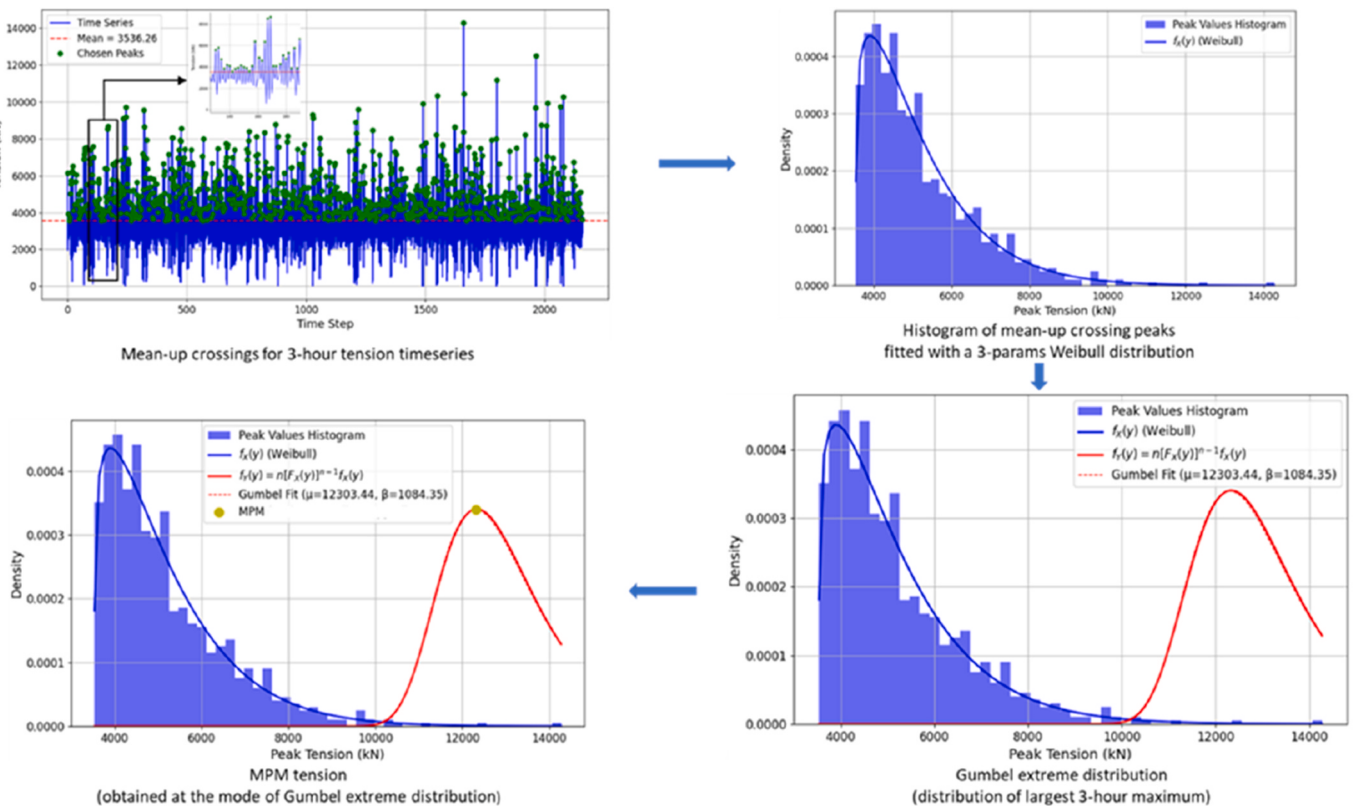


Fig. 2. Steps to calculate MPM from the time history of the line tension of one seed.

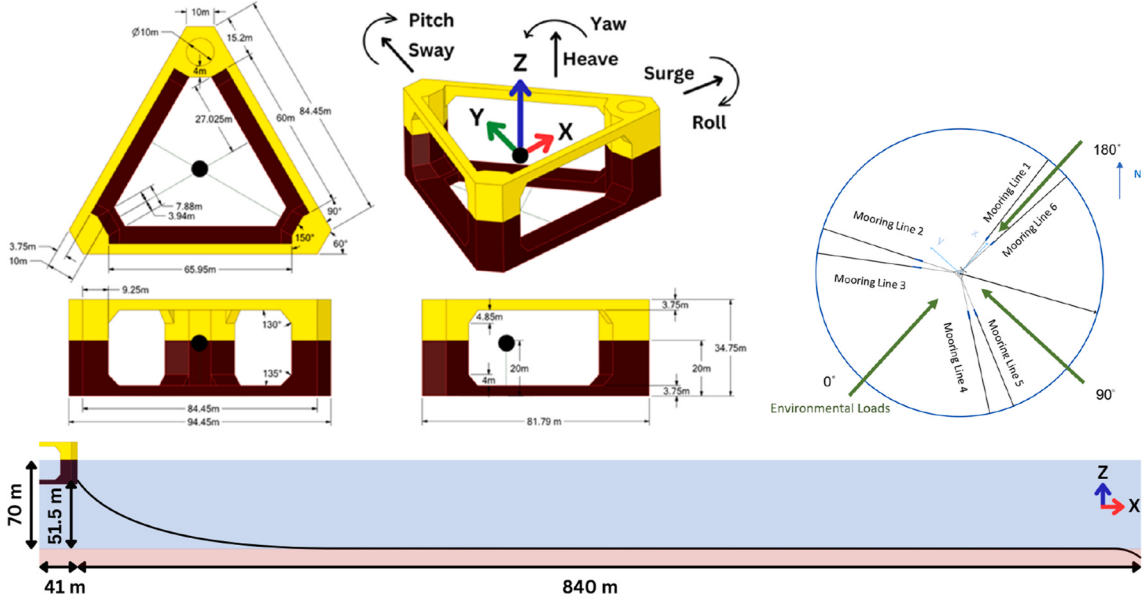


Fig. 3. TaidaFloat dimensions and a 3x2 mooring configuration as an example.

Table 1

Principal dimension of IEA 15 MW wind turbine.

Turbine	Mooring		
Rotor configuration	Upwind, 3 blade	Water depth	100 m
Rotor diameter	240 m	Mooring radius	840 m
Hub height	150 m	Chain grade	R4S
Blade mass	65.25 t	Breaking load	24764 kN
Tower mass	1263 t	Pretension	7 % MBL
RNA mass	991 t	Line length	806 m
Cut-in/Rated/Cut-out wind speed	3/10.59/25 m/s	Wet weight	575 kg/m
Cut-in/Rated rotor speed	5/7.56 RPM	Stiffness	2468000 kN
Shaft Tilt/Pre-cone angle	6/4°		

$$k_{11} = \frac{P}{\operatorname{arccosh}\left(\frac{ph}{Th} + 1\right) - \left(2 \sqrt{1 + 2 \frac{Th}{ph}}\right)} \quad (17)$$

An interpretation of the above equation is that, as the horizontal environmental force acting on the floater increases (or equivalently, as the offset increases), the horizontal mooring stiffness also increases. This implies that at a higher offset state, a greater horizontal force - or, equivalently, higher mooring line tension - is required to induce the same incremental horizontal displacement. This nonlinear behaviour reflects the geometric stiffness characteristic of catenary mooring systems and is well illustrated in Fig. 4 with the surge offset vs restoring force graph. Furthermore, at a given offset, the  $3 \times 3$  mooring configuration provides the largest restoring force, suggesting an improved ability to resist displacement. This may imply that the  $3 \times 3$  system offers better control over the floater's position compared to the other configurations. More about influence of mooring parameters on the stiffness curves can be found in (Chen et al., 2024).

#### 4. Regions with tropical cyclones

There are six tropical cyclone (TC) basins worldwide, commonly classified as the North Atlantic (NA), Western Pacific (WP), Eastern Pacific (EP), South Pacific (SP), North Indian (NI), and South Indian (SI). The tropical cyclones of each basin have distinct climatological and

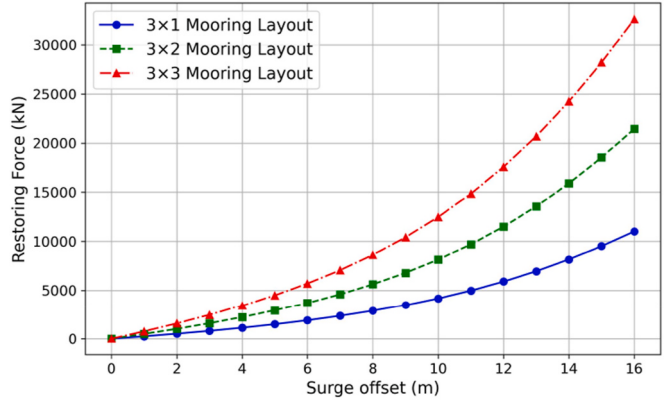
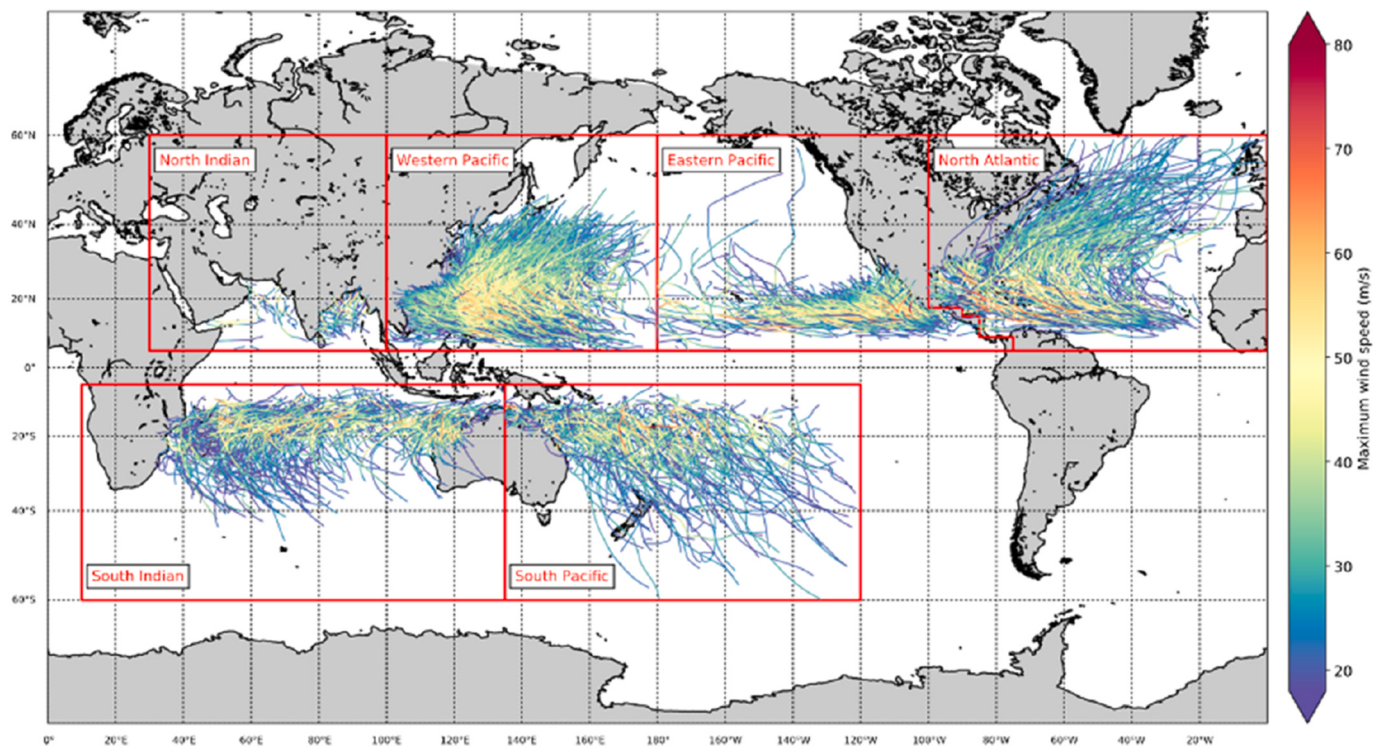


Fig. 4. Mooring X direction (surge) restoring force at different surge offsets (stiffness curve).

formation mechanisms. Grossmann-Matheson et al. (2024) (Grossmann-Matheson et al., 2024) pointed out that differences in TC tracks, storm frequency and distribution of TC wind field for each tropical cyclone basin led to variations in extreme met-ocean conditions. Fig. 5 presents the location of different tropical cyclone basins, the track, and intensities of the tropical cyclones from 1980 to 2018 (Bloemendaal et al., 2020a).

In the following, we want to explain the characteristics of the frequency of TCs and characterise wind and wave conditions. From Fig. 5, we can qualitatively understand that the Western Pacific and North Atlantic regions have experienced more typhoon or hurricane strikes. Table 2 gives a more detailed statistics of the frequency of TCs in each basin, presents the number of tropical cyclones from 1979 to 2008 with 10-min maximum wind speed exceeding 17.5 m/s. Based on the data by World Meteorological Organisation (World Meteorological Organization, 2017), 29.8 % of tropical cyclones occur in the Western Pacific basin, 18.6 % in the Australian region (including the Southeast Indian and Southwest Pacific basins), and 13.2 % in the North Atlantic. The high proportion of severe tropical cyclones in the Western Pacific basin suggests that floating wind turbines in this region are subject to more frequent and intense loading conditions. Therefore, understanding the structural responses in this basin is critical for developing resilient



**Fig. 5.** The location of different basins and the track, and the intensities of the tropical cyclones (Bloemendaal et al., 2020a).

**Table 2**

The number of tropical cyclones from 1979 to 2008 with maximum wind speed exceeding 17.5 m/s (Bloemendaal et al., 2020a).

North Atlantic	Easter Pacific	Western Pacific	North Indian	South Indian	South Pacific
355	491	803	148	396	502
13.2 %	18.2 %	29.8 %	5.5 %	14.7 %	18.6 %

designs. In contrast, tropical cyclone basins with lower cyclone activity may require different considerations, making comparative analysis across basins essential.

The extreme wave and wind conditions have unique characteristics, especially when we focus on a particular region of interest. According to Grossmann-Matheson's 2004 study (Grossmann-Matheson et al., 2024), the 100-year return period significant wave height at the Taiwan Strait ( $24.55^{\circ}\text{N}$ ,  $119.45^{\circ}\text{E}$ ) is 15.57 m. In contrast, 100 km offshore from Wakayama, Japan ( $32.55^{\circ}\text{N}$ ,  $134.45^{\circ}\text{E}$ ), the corresponding value is slightly higher at 16.45 m. In the North Atlantic, the 100-year return period significant wave height at the Gulf of Mexico ( $27.55^{\circ}\text{N}$ ,  $90.55^{\circ}\text{W}$ ) is 13.84 m, notably lower than in the Western Pacific. N Bloemendaal (2020) (Bloemendaal et al., 2020b) estimated global tropical cyclone wind speeds. According to his study, the 100-year return period wind speeds (10-min average at 10-m) at Taipei and Tokyo (both in the Western Pacific) are approximately 55.0 m/s and 34.5 m/s, respectively, while at Miami (in the North Atlantic), it is about 59.5 m/s. Interestingly, the Taiwan Strait experiences higher wind speed than the coast near Japan, but has a lower significant wave height. Similarly, the Gulf of Mexico (in the North Atlantic) exhibits wind speed comparable to that of the Taiwan Strait but with lower wave height. These phenomena can be explained by the physical processes of cyclone intensification, weakening and propagation.

Cyclones drive energy from the ocean's surface evaporation, with the latent heat released during condensation fuelling their development. Higher Sea Surface Temperature (SST) enhances evaporation, promoting more intense cyclones, causing the cyclone to weaken and wind

speeds to diminish. This explains why the Taiwan Strait tends to experience stronger wind speeds than the coast near Japan. Wave height is primarily influenced by the maximum wind velocity  $V_{max}$  and the velocity of forward movement of the tropical cyclone  $V_{fm}$  (Grossmann-Matheson et al., 2024). A higher  $V_{fm}$  allows waves to remain within the cyclone's intense wind field for longer, which enables waves to absorb more energy from the wind and grow larger. In the Western Pacific,  $V_{fm}$  tend to increase at higher, sustaining the wave growth and resulting in more extreme significant wave height along the southern coast of Japan (Grossmann-Matheson et al., 2024). In contrast, although the North Atlantic experiences stronger cyclones, their frequency is much lower and  $V_{fm}$  is smaller than the Western Pacific's, particularly in the Gulf of Mexico. Consequently, the extreme wave heights in the Gulf of Mexico are lower than those in the Western Pacific (Grossmann-Matheson et al., 2024). Given the unique characters of met-ocean conditions across different tropical cyclone regions, it is crucial to account for the variations in wind speed, wave height and wave period when assessing the impact of extreme met-ocean conditions on floating wind turbines.

To investigate the impact of extreme metocean conditions in different tropical cyclone basins on floating wind turbine performance, mooring analyses were conducted in the Taiwan Strait, Japan's Ise Bay (both in the Western Pacific), the Gulf of Mexico (North Atlantic), and Northwest Australia (South Indian). For comparison, two non-tropical cyclone regions—the North Sea and Western Africa—were also included. The North Sea is a shallow shelf sea with a mean depth of 80 m, and its metocean condition is influenced by its shallow depth, resulting in strong winds, harsh waves, and currents. In contrast, the metocean conditions of Western Africa are relatively calm and dominated by swell with a longer wave peak period compared to other regions.

## 5. Metocean conditions for cyclone and non-cyclone regions

In this study, five regions with distinct extreme metocean conditions were selected for mooring analysis. These include three tropical cyclone regions: the Taiwan Strait/Japan's Ise Bay, the Gulf of Mexico, and

Northwest Australia, and two non-tropical cyclone regions: the North Sea and West Africa. The extreme metocean conditions used in this study and corresponding references are presented in [Table 3](#).

Both DNV ([Det Norske Veritas, 2024](#)) and IEC ([International Electrotechnical and Commission, 2025](#)) design criteria specify a 50-year return period as the standard requirement for offshore wind turbine design. Although the API ([API, 2005](#)) standard allows for different return periods depending on the consequence level, a 50-year return period is consistently required for medium-consequence structures (L-2 level), aligning with IEC and DNV requirements. Wind speed is defined as a 1-h average wind speed at 10 m above sea level, which aligns with the requirement of ISO 19901-1 ([Organisation, 2015](#)), API, and DNV. The sea surface is assumed to be stationary for a duration of 3 h.

In [Table 2](#), the return period for load cases 4 and 6 is 100 years, while the surface current speed in load cases 2 and 5, as well as the wave peak period in load cases 2 and 3, are not provided. The following methods are applied to convert the 100-year return period to a 50-year return period and to estimate the missing values of wave peak periods and surface current speeds.

### 5.1. Return period conversion

[Equations \(18\)–\(20\)](#), adopted from standard “EN 1991-1-4” ([European Committee for Standardization CEN, 2004](#)), is used to convert extreme conditions from a 100-year return period to a 50-year return period:

$$X_T = c_{prob} \times X_{T_0} \quad (18)$$

$$c_{prob} = \sqrt{\frac{1 - K \cdot \ln \left[ -\ln \left( 1 - \frac{1}{T} \right) \right]}{1 - K \cdot \ln \left[ -\ln \left( 1 - \frac{1}{T_0} \right) \right]}} \quad (19)$$

$$K = 0.2 \quad (20)$$

[Equations \(18\)–\(20\)](#) express the probabilistic conversion coefficient  $c_{prob}$ , based on the Gumbel distribution, to adjust extreme values between different return periods. For the conversion from a 100-year to a 50-year return period,  $T_0 = 100$  and  $T = 50$ , resulting in a coefficient

$$c_{prob} = \sqrt{\frac{1 - 0.2 \cdot \ln \left[ -\ln \left( 1 - \frac{1}{50} \right) \right]}{1 - 0.2 \cdot \ln \left[ -\ln \left( 1 - \frac{1}{100} \right) \right]}} = 0.9792.$$

### 5.2. Wave peak period and surface current speed estimations

S. A. Hsu ([2023](#)) ([Hsu, 2015](#)) proposed a relationship between significant wave height  $H_s$  and wave peak period  $T_p$  during tropical cyclones, which can be expressed as:

**Table 3**  
The extreme metocean conditions.

No., Ref.	Regions	Wind speed (m/s)	Significant wave height (m)	Wave peak period (s)	Surface current speed (m/s)	Return period (years)
1 ( <a href="#">Wang et al., 2002</a> )	West Africa	14.0*	4.7*	22.0*	0.3*	100
2 ( <a href="#">Wen et al., 1991</a> )	Gulf of Mexico	42.5	10.7	—	1.6	50
3 ( <a href="#">Hsu et al., 2022; Central Weather Administration ROC (Taiwan) Ministry of Transport, 2024</a> )	Taiwan strait	42.32	12.7	11.8	1.59	50
4 ( <a href="#">Li et al., 2015</a> )	North Sea	33.6	13.4	13.1	—	50
5 ( <a href="#">Xia et al., 2012</a> )	West Australia	33.5*	14.0*	14.5*	0.95*	100
6 ( <a href="#">Aichi Prefecture Coastal Protection Basic Plan Review Committee, 2023</a> )	Japan Ise bay	36.8	14.4	—	—	50

The values marked with \* should be converted to correspond to a 50-year return period.

The ‘\*’ indicates that it requires supplementation.

$$T_p = 5.3 \times H_s^{0.4} \quad (21)$$

[DNV-RP-C205 \(Norske Veritas, 2025\)](#) provides a method for estimating surface current speed based on wind speed. The wind-induced surface current speed can be calculated using the following equation:

$$V_{c,wind} = kU_{10m} \quad (22)$$

Where  $U_{10m}$  is the mean wind speed at a height of 10 m, and  $V_{c,wind}$  is the surface current speed. The coefficient ranges from 0.015 to 0.03. In this study, the average value is adopted. Here, we neglect the tidal currents, as they are considered small in a water depth of 100 m.

By applying equations in 4.1 and 4.2, the updated extreme metocean conditions are obtained and presented in [Table 4](#), which will be used for the subsequent FOWT simulations.

[Fig. 5](#) represents the wind and wave spectrum of all selected regions: North Sea, West Africa, Gulf of Mexico, West Australia, Japan and Taiwan Strait. The JONSWAP spectrum is adopted in this study due to its suitability in representing typhoon-associated sea states ([Hasselmann et al., 1980](#)). For wind conditions, the NPD wind spectrum is utilised in accordance with API RP 2A-WSD specification ([API, 2005](#)). This spectrum characterizes turbulent wind loading by introducing stochastic variation in wind speed over time, while maintaining a fixed direction. The spectral shape inherently captures the turbulence energy distribution across frequencies and includes the effects of turbulence intensity as defined in the standard. This model was implemented using the built-in wind spectrum options in OrcaFlex, which follows the same formulation as described in the API specification.

Based on the environmental parameters presented in [Figs. 6](#) and [Table 4](#), the Taiwan Strait and the Gulf of Mexico (GoM) exhibit the most severe wind conditions, followed by Japan, the North Sea, and Western Australia, in descending order. In contrast, with regard to wave severity,

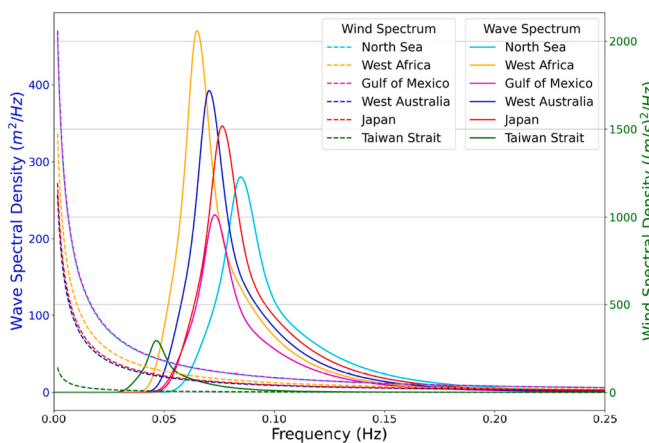
**Table 4**  
The updated extreme metocean conditions.

No.	Regions	Wind speed (m/s)	Significant wave height (m)	Wave peak period (s)	Surface current speed (m/s)	Return period (years)
1	West Africa	13.7	4.6	21.5	0.29	50
2	Gulf of Mexico	42.5	10.7	13.7	1.6	50
3	Taiwan strait	42.32	12.7	11.8	1.59	50
4	North Sea	33.6	13.4	13.1	0.83	50
5	West Australia	32.8	13.7	14.2	0.93	50
6	Japan Ise bay	36.8	14.4	15.4	0.76	50

**Table 5**

Floater motions and Tower Bending Moment results for collinear | directional load cases, in % of global average of maxima respective parameter across all load directions.

Regions ranked by wave height	Surge	Heave	Pitch	Yaw	Tower Bending Moment	Mooring Line Tension
Global average of maxima	17.7   16.5 m	5.15   5.13 m	7.32   7.36 °	9.94   9.59 °	753   730 MNm	11.3   10.6 MN
West Africa	34   34 %	72   73 %	82   81 %	21   22 %	52   53 %	52   27 %
Gulf of Mexico	119   120 %	84   85 %	99   102 %	131   129 %	111   108 %	105   101 %
Taiwan strait	140   139 %	100   101 %	95   94 %	133   134 %	118   120 %	142   136 %
North Sea	100   101 %	107   106 %	87   87 %	101   100 %	91   87 %	92   91 %
West Australia	97   97 %	107   107 %	103   103 %	97   97 %	99   101 %	96   95 %
Japan Ise bay	110   110 %	129   128 %	134   133 %	116   118 %	129   131 %	113   112 %

**Fig. 6.** Wind and Wave spectrum.

Japan experiences the highest wave conditions, followed by Western Australia, the North Sea, the Taiwan Strait, and GoM. Most sites show peak spectral periods in the range of 13 s–15 s. The wave spectrum reveals two distinct frequency bands: the wave frequency (WF) region, spanning 4–20 s (0.05–0.25 Hz), and the low-frequency (LF) region, defined by components with periods exceeding 20 s (i.e., frequencies <0.05 Hz). Although West Africa exhibits a relatively long peak period of approximately 21 s, the accompanying low wave height and modest wind speed suggest that mooring loads are minimal, rendering it a low-priority site compared to other areas. Consequently, the subsequent analysis focuses on the remaining regions with harsher environmental conditions, where the decomposition into WF and LF components is critical for evaluating platform responses to first- and second-order wave loads, as well as to wind- and current-induced forces.

Note that metocean conditions are site-specific, and spatial variation cannot be neglected near the coast (Wada et al., 2018). The extreme conditions provided in Table 4 serve as typical values grounded in well-established academic sources, for comparative study of the five regions. Also note that the conditions do not account for the uncertainty of extreme value estimation, which can be significant for tropical cyclone events with a small sample size (Jonathan et al., 2013; Wada et al., 2016).

While DLC 1.6 is often considered critical in many regions, for this high wind-speed typhoon environment, DLC 6.1 was found to produce the governing loads in a previous study (Ivanov et al., 2024b), and is therefore adopted in this analysis. A previous study also showed that ULS (Ultimate Load State) is driving mooring design in shallow water and not FLS (Fatigue Load State) (Huang and Yang, 2021).

## 6. Mooring tensions and floater motions

The mooring tension computed with OrcaFlex for the six studied regions is shown in Fig. 7. Among the studied locations, the Taiwan Strait exhibits the highest peak mooring tension, indicating it is the most demanding region in terms of mooring load, while West Africa shows the lowest, suggesting relatively benign conditions. Japan consistently ranks as the second most severe region, followed by the Gulf of Mexico, West Australia, and the North Sea. Notably, elevated tensions are observed at 30° and 150°, which can be attributed to yaw-induced asymmetry and the varying number of mooring lines oriented toward the environmental load direction (Ivanov et al., 2024a).

To analyse the impact of environmental conditions on mooring tension, we categorise the sources of mooring tension into two components: steady-state tension and dynamic tension. Though environmental load direction does have an impact on LF response and thus the mooring tension. Fig. 7 reveals that the relative proportions of these two components remain consistent across different environmental angles within the same region. Therefore, the upcoming analysis is conducted based on the environmental direction of 0° only, as illustrated in Fig. 8 (left), which shows the MPM mooring tension across various regions, consisting of steady-state tension and dynamic tension as the two main components. The environmental loads acting on the floater can be divided into 3 components: steady-state load, low-frequency load, and wave-frequency load. The steady state load includes responses from constant magnitude and direction forces, such as current, mean wind, and mean wave drift forces. The low-frequency load is imposed by wind loads, slow-varying wave drift forces, and current loads. Fig. 8 (left) presents the steady-state force components for each region under a 0-degree environmental load direction. The steady-state forces acting on the floater and mooring system generate corresponding steady-state tensions, while the dynamic tensions are influenced by the low-frequency and wave-frequency forces.

A clear correlation can be observed between steady-state mooring tension and steady-state environmental loads, with the results grouping into three tiers. The Taiwan Strait and the Gulf of Mexico exhibit the highest steady-state mooring tensions, followed by Japan, Western Australia, and the North Sea. West Africa consistently shows the lowest tension levels. Among the contributing forces, wind consistently emerges as the dominant component of the steady-state load, followed by current, and finally wave drift forces. The magnitudes of wind and current forces generally follow the same order as their respective velocities. Meanwhile, the mean wave drift load is highest for the Taiwan Strait. This can be attributed to the second-order wave force (QTF) data being higher at the Taiwan Strait's wave peak period (~12 s) and lower in other regions.

Among wave, wind, and current forces, what is the proportion of their influence on mooring line tension? While everyone hoped for an easy answer, unfortunately, none can be given. Fig. 8 (left) reveals the proportions of force contributions in steady state (static) simulation. Waves have minimal effect, while wind dominates in every region.

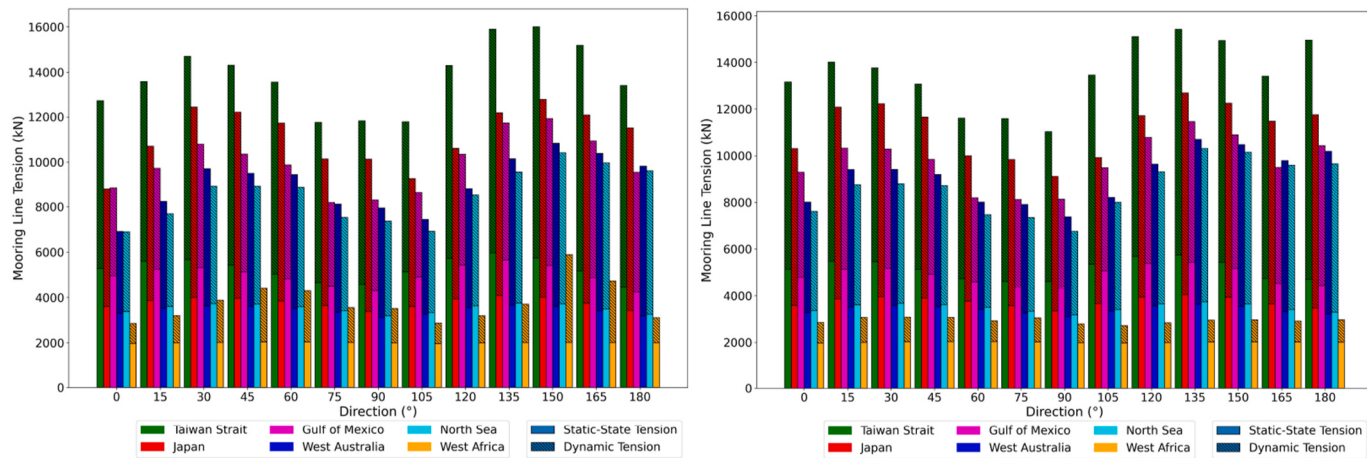


Fig. 7. The MPM mooring tension comparison of six regions: collinear (left) and directional (right).

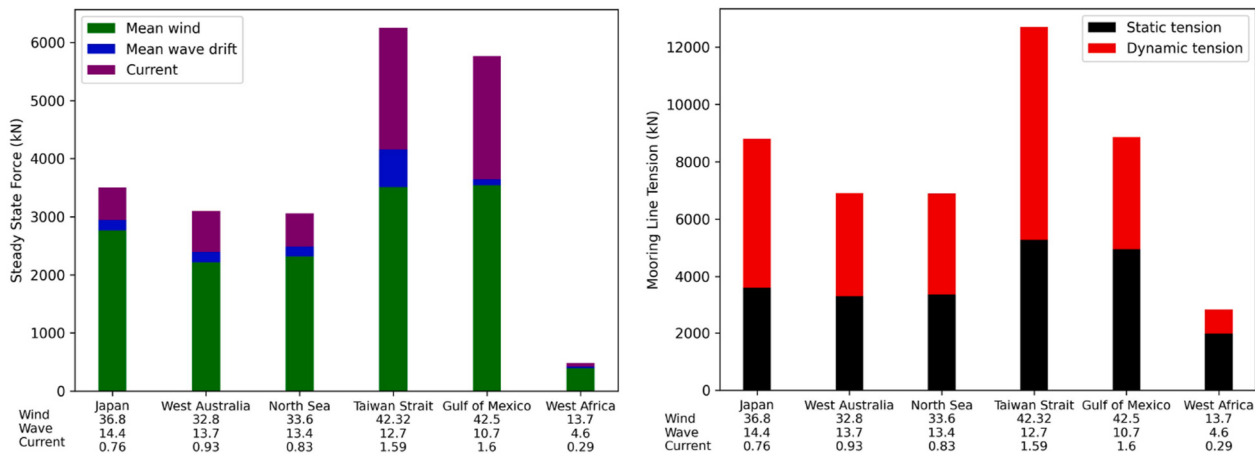


Fig. 8. Steady-state force components in each region (left) and mooring tension (right); under 0° collinear environmental loads.

However, this is not true for the dynamic tension.

Consider the Taiwan Strait and the Gulf of Mexico – same wind and current speeds, but wave height is different; still, the steady state tension is almost the same. On the other hand, Taiwan Strait's dynamic tension is 57 % higher than GoM's, the wave height is only 19 % higher, a 3 %

tension increase for each 1 % of wave height. Instead, compare Japan with West Australia: 12 % smaller current and 12 % faster wind roughly cancel each other out, leaving the 5 % difference in wave height; it resulted in 22 % larger tension, 4.4 % per 1 % of wave height increase. So, the same increase in wave height produces a different increase in

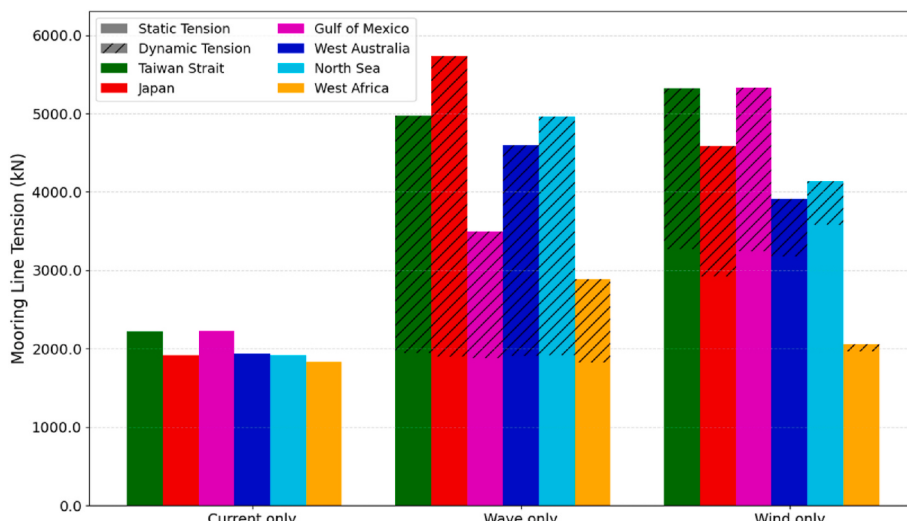


Fig. 9. Static and dynamic mooring tension under 0° of wind/wave/current only load.

tension – these numbers only give us a hint, not the answer. To understand how and why, we delve into the physical reasons behind wind-wave interaction in Chapter 7.3.

[Fig. 9](#) introduces static and dynamic mooring tension under 0° of wind/wave/current only load.

A uniform current induces minimal dynamic tension in the mooring lines. While higher current speeds lead to increased mooring tension, the differences across cases remain relatively small. Wind effects are quite straightforward: higher wind speeds result in increased static and dynamic mooring tensions. For wave-induced static tension, only minor variations are observed across different environmental conditions. This can be attributed to the relatively small mean wave drift forces, as shown in [Fig. 8](#). Wave-induced static tension is also smaller than wind in all conditions indicating the role of wind in forming the steady-state tension. Dynamic tension in wave is not that intuitive as we can see Taiwan Strait with the significant wave height only ranked fourth having the second highest mooring tension. This observation indicates the importance of the peak spectral period in exciting the motion at platform's natural frequency.

Now consider West Australia and the North Sea, the former's wave height is 2 % larger and wind speed is the same, resulting in a 7 % dynamic tension increase. According to the last paragraph, a 2 % increase in wave height contributes to a 6–9 % increase in tension. Sounds right until you consider the significant 22 % difference in current speed – does it have no effect? It does have, but an indirect one, as we show in Chapter 7.1.

It is evident that no single environmental parameter - such as wind speed, wave height, or current velocity - can independently determine the mooring tension ranking. Instead, mooring response arises from the combined and interacting effects of wind, wave, and current forces. The roles and interactions of these components are further examined in the next chapter.

Apart from mooring tension, maximum values of the floater motions and the total bending moment (TBM) at the bottom of turbine's tower are important design parameters. Particularly, Tower Bending Moment is a major constraint in FOWT structural design ([Ivanov et al., 2023; Zou et al., 2022](#)). From the results of OrcaFlex analyses, [Table 5](#) presents the values in % of global average of maxima, which is calculated by first finding the maximum value of a parameter across all load directions (0–180°) for each region and then averaging across all regions.

The colours help to see the trend highlighting worst values in dark orange and best in dark green. It highlights two correlations: (i) surge and yaw driving drive the mooring line tension and (ii) pitch driving the tower bending moment and coupling with heave motion. Heave motion is independent of wind and correlates directly with wave height; pitch is highly influenced by both wind and wave, while surge and yaw are mostly influenced by the wind. These observations are consistent with current science on floater motions ([Ma et al., 2019](#)). This paper focuses on discussing the FOWT mooring line tension, and it is evident that it is highly influenced by wind and somewhat less by waves, unlike oil rigs' moorings which are primarily constrained by waves. Noteworthy, the region with the highest mooring tension (Taiwan Strait) does not coincide with the highest TBM region (Japan Ise Bay), shedding light on why Japan's demo FOWTs faced turbine-related challenges ([Rui and Wen, 2020](#)). It can be said that extreme wind speed is the major design constraint for the mooring system, while wave height is the major design constraint for the floater structure and its connection to the turbine tower.

Regarding collinear and directional loading conditions, the colour trend is the same and there is barely any difference for all parameters expect for mooring line tension, where directional approach always results in mildly or even drastically lower tension, further explained in the conclusion.

## 7. Assessments on wind, waves, and currents interactions

### 7.1. Current-wave interaction

To isolate and evaluate the influence of current with wave on mooring system behaviour, time-domain simulations were performed under two environmental scenarios: (1) waves only, and (2) combined waves and current. Additionally, the effects of wave-current interaction were considered through the inclusion of wave drift damping. Therefore, the combined wave and current case was further subdivided into scenarios with and without wave drift damping. The environmental conditions were derived from the Taiwan Strait metocean data ([Table 4](#)) and the analysis focused on the 0° environmental heading. This alignment was chosen for simplification, ensuring that the dominant platform motion was in the surge direction. This setting will also be used when discussing wave-wind or current-wind interaction.

[Fig. 10](#) (right) presents the statistical analysis of mooring line tension, current-induced force, and 2nd order (wave drift) force across the three conditions. The upper and lower whiskers denote the maximum and minimum observed values, respectively. The central rectangle spans one standard deviation above and below the mean, while the mean itself is marked by a black dot. Complementing this statistical overview, [Fig. 10](#) (right) also displays the Power Spectral Density (PSD) of mooring line tension for the three conditions as well as a snapshot of surge and mooring tension timeseries.

The inclusion of current, particularly with wave drift damping, leads to a significant increase in mooring tension, nearly doubling its magnitude compared to the wave-only case. A similar trend is observed in the second-order wave (drift) force. The PSD and timeseries plots further reveal that this increase is primarily concentrated in the LF region (WF surge observed no changes at all), where 2nd order wave loads and current-induced forces dominate. Since the 1st order wave loading remains unchanged across all cases, the amplification in mooring tension can be attributed to the combined effect of enhanced wave drift forces and the introduction of LF current-induced forces.

Another key observation from the timeseries is that the current-induced force, despite originating from a uniform flow, exhibits temporal variation and is excited at the system's surge natural frequency due to its dynamic coupling with wave-induced platform motions. As formulated in Equation (13), the magnitude of the current force is proportional to the platform's LF surge velocity. Consequently, when wave drift forces - amplified through wave-current interaction - increase LF motion amplitude, the current force develops cyclic loading at similar frequencies. This feedback mechanism intensifies the platform's LF surge response, further amplifying mooring tension and explaining the elevated spectral peaks at the surge natural frequency when wave drift damping is included.

Without wave drift damping, the wave drift force shows negligible differences between the "wave only" and "wave + current" cases, both in terms of statistical values and spectral characteristics. This aligns with expectations, as wave-current interaction effects are captured through the drift damping mechanism. Without it, wave drift and current forces remain independent. Under these conditions, the increase in mooring tension stems solely from the current-induced force. Although the current force itself is smaller in magnitude - its maximum value is approximately 8 % of that of the first-order wave force and 33 % of the second-order wave drift force - its influence on the mooring system is significant. By exciting at the surge natural frequency, it contributes to a 33 % rise in mooring tension, from around 6000 kN in the wave-only case to nearly 8000 kN when current is included.

### 7.2. Current-wind interaction

The effects of wind and current can also be investigated by comparing time-domain simulations performed under two environmental scenarios: (i) wind only, and (ii) combined wind and current.

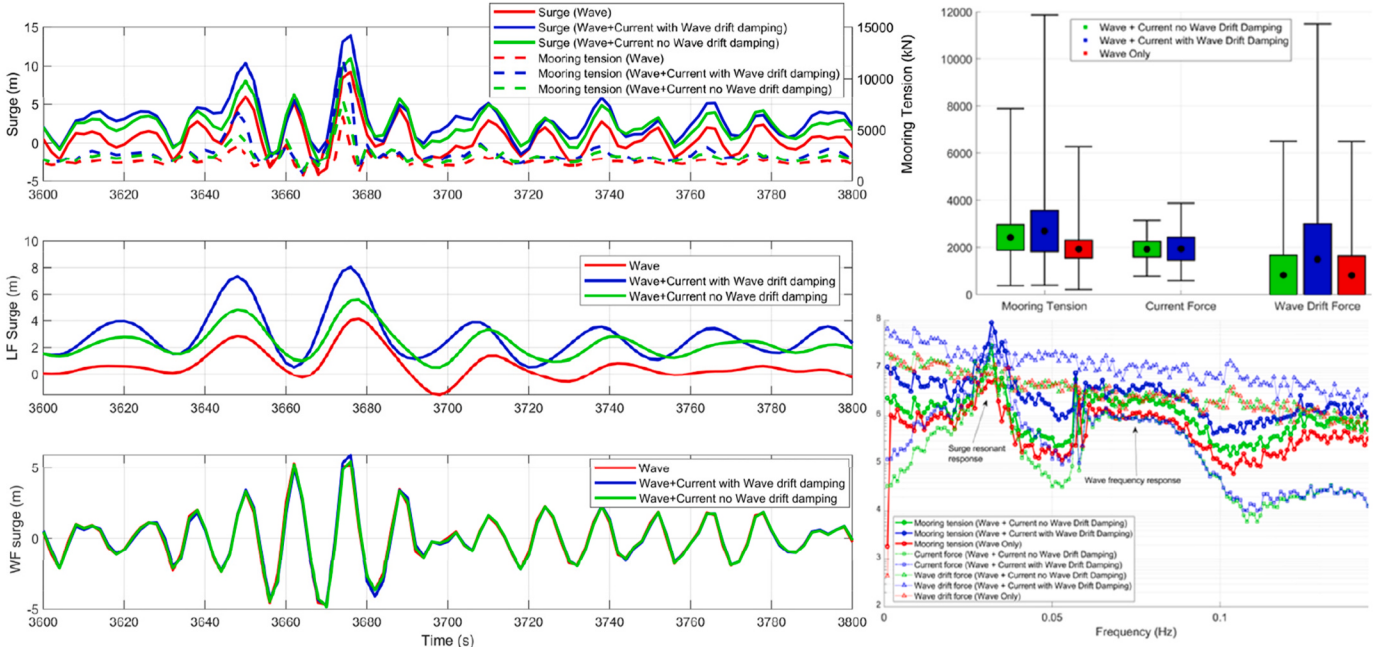


**Fig. 10.** Left: Timeseries of mooring tension, surge; LF surge and WF surge under wave only; wave and current with and without wave drift damping. Right: Statistical values and PSD chart.

**Fig. 11 (left)** presents the statistical analysis of mooring line tension, current-induced force, and wind-induced force for the two conditions. **Fig. 11 (right)** displays the PSDs and the timeseries graphs of surge and mooring tension.

An increase in the average mooring tension and minimum tension is again observed with the inclusion of current, reflecting a higher mean offset of the floating structure. However, unlike previous cases, the increase in maximum tension is more moderate, rising by approximately 25 %, from 4000 kN to slightly over 5000 kN. The current-induced force, although arising from a uniform flow, continues to exhibit temporal variation and is excited at the system's surge natural frequency, as shown in **Fig. 11 (right)**, due to its dynamic coupling with wind-induced LF platform motions. The more moderate increase in mooring tension

can be explained by the geometric stiffness characteristics of the mooring system, which exhibits a nonlinear relationship between surge displacement and horizontal restoring force (or mooring tension), as shown in **Fig. 3**. The inclusion of current results in a surge offset increase of about 2m for all cases. Although the wave-induced LF surge offset is smaller than that induced by wind (approximately 4 m vs. 6 m at the time of maximum tension), the superposition of WF motion in the wave-only case leads to a surge displacement rising from 9m to 11m, while in the wind-only case, it increases from 6m to 8m. This disparity in initial and peak surge displacement, when viewed alongside the nonlinear behavior between mooring tension and surge displacement, explains the observed differences in mooring tension escalation. While this interpretation is quasi-static (assuming mooring tension depends primarily

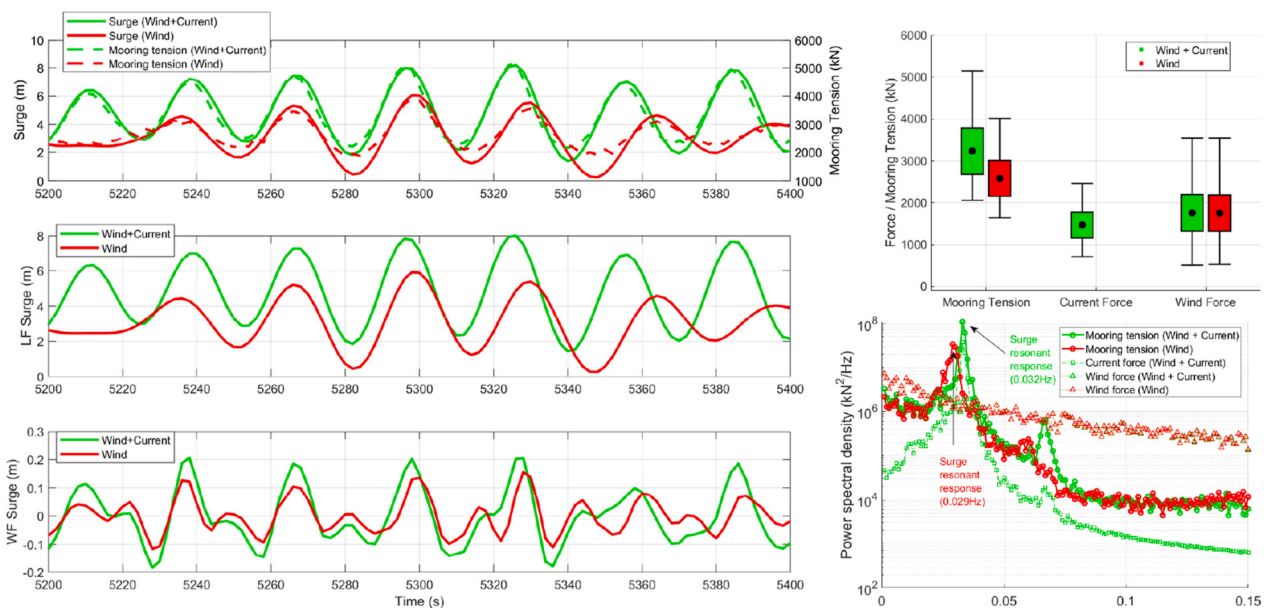


**Fig. 11.** Left: Timeseries of mooring tension, surge; LF surge and WF surge under wind only and current with wind conditions. Right: Statistical values and PSD chart.

on the floater's fairlead position, it remains valid, as the inclusion of current predominantly excites LF components. According to (Ma et al., 2019), quasi-static analysis is appropriate for estimating mooring responses driven by mean offset and LF motions.

Both wind and current forces are active primarily in the LF region (barely any WF surge is seen in Fig. 11). The wind force remains largely governed by the wind speed, as evidenced by the close trend between the wind force PSD and the wind energy spectrum. Its spectral content remains mostly unchanged between with and without the inclusion of current (or wave as shown in the next section). We can see that the variations in platform motion or surge speed from current (or wave) are small relative to the magnitude of wind velocity typical of typhoon conditions. As a result, no significant changes in wind force are observed in the statistical data.

In the absence of wave force, the presence of current increases the steady-state offset of the platform, leading to a tauter mooring system with greater stiffness, which in turn shortens the surge natural period. This behaviour was previously obscured in wave-inclusive simulations, where the dominance of wave forces masked the influence of current. However, under wind and current conditions this shift in the natural period becomes more discernible.

### 7.3. Wind-wave interaction

The effects of wind and wave can also be investigated by comparing time-domain simulations performed under three environmental scenarios: (i) wind only, (ii) wave only and (iii) combined wind and wave. Note that the wind condition is the same as that of section 7.2. Fig. 13 shows the necessary results under three conditions: wave, wind and wind with wave.

A black solid window is seen on the tension timeseries in Fig. 13 – it shows that when wind and wave forces are in-phase, their contributions to mooring tension are cumulative, resulting in the highest peak tensions. Conversely, when wind and wave forces act in opposing directions, the wave does not induce much tension, and total tension is almost the same as wind-only tension. Interestingly, that is different from wave superposition, as waves add together in-phase, but no cancellation occurs out-of-phase. This is evidenced in the counter-phase portion of Fig. 13 (dashed line window). This can be explained and understood by examining Fig. 12. Consider that both wind and wave are moving the floater to the right, and their force magnitude independently varies with time. When wave and wind arrive during a period of minimal offset - corresponding to low horizontal mooring stiffness, as illustrated in Fig. 3 - it can rapidly accelerate the floater toward a position of higher displacement. However, as the floater's displacement increases, the horizontal mooring stiffness also increases, providing greater restoring force and thereby limiting further wave-induced and wind-induced motion. A perfect wind-wave phase match can happen during extreme weather conditions; however, the probability of in-phase occurrence of all wind and wave components would be extremely rare since they all span across a range of frequencies. Forcing an irregular sea state, with

different wave components to be in-phase with all wind components, would be too conservative for maximum tension calculation, however many “close to resonance” peaks occur naturally.

Wind and wave forces act largely independently. As previously noted, wind force remains primarily governed by wind speed. However, wind-induced mooring tension exhibits periodic oscillations that are only very slightly affected by variations in wind speed – instead, they are in-phase with the surge motion, with an observed oscillation period of approximately 34–36 s. This periodicity aligns with the peak identified in the surge RAOs in Fig. 12 (centre). In contrast to current-inclusive simulations, the wave drift force (and 1st order wave force) also shows no significant change in either statistical measures or spectral characteristics upon the addition of wind, indicating minimal coupling between wind and wave drift contributions.

Statistical analysis also reveals that wind induces higher mean mooring tensions than waves, keeping the system in a more consistently loaded state. On the other hand, wave-induced WF motions introduce smaller, high-frequency fluctuations superimposed on the baseline tension established by wave drift-induced LF motions. As illustrated in Fig. 13 (2nd subplot), the LF motions driven by wave drift forces are generally lower in magnitude than those induced by wind, which helps explain the higher mean mooring tensions under wind loading.

We note that the simulated 2nd order wave force results are in good agreement with tank test results, which showed that the 2nd to 1st order wave force ratio varies from 0.6 % to 14.9 %, with an average of 7.2 % (Haocheng et al., 2025).

## 8. Conclusions

Six locations popular for offshore development were analysed, including four regions known for their severe cyclones/hurricanes/typhoons; the results are summarized in Fig. 14. Among these, the Taiwan Strait is by far the most challenging and expensive environment for mooring: even if the largest producible chain diameter of 220 mm is used for future projects, it requires a 3x3 mooring system, while benign West Africa can use a 3x1 pattern. The required mooring patterns using non-collinear loads and the current practical limit of 170 mm chain are shown in Table 6, considering corrosion allowance. Note that a 3x1 system is generally difficult to achieve as a safety factor of 2.0 is required (e.g., by ABS (ABS, 2020)), while only 1.67 is required for other configurations, as they are redundant.

It was found that dynamic tension is the main difference between environments. It is mostly influenced by wave height, but amplified by wind and current, as shown in the Results section. One of the lessons learned is that if the wave height is low (e.g. in West Africa), static simulations might be good enough for preliminary mooring analyses, saving computational effort. It is important to note that these dynamic tensions can be critical to mooring designs as they are the main cause for mooring line fatigue failure (Ma et al., 2013). As for steady-state (static) tension, all six regions experience this same trend of contribution order: wind, currents, and then waves. Among the six regions, Taiwan Strait

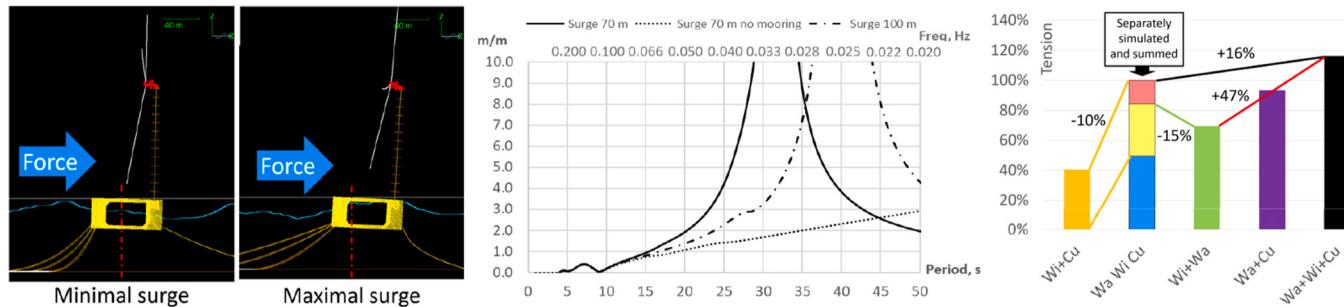


**Fig. 12.** Left: Floater surge movement by wind and wave forces. Centre: Surge RAOs for 2 depths (no surge damping) Right: Forces interaction effect on maximum tension.

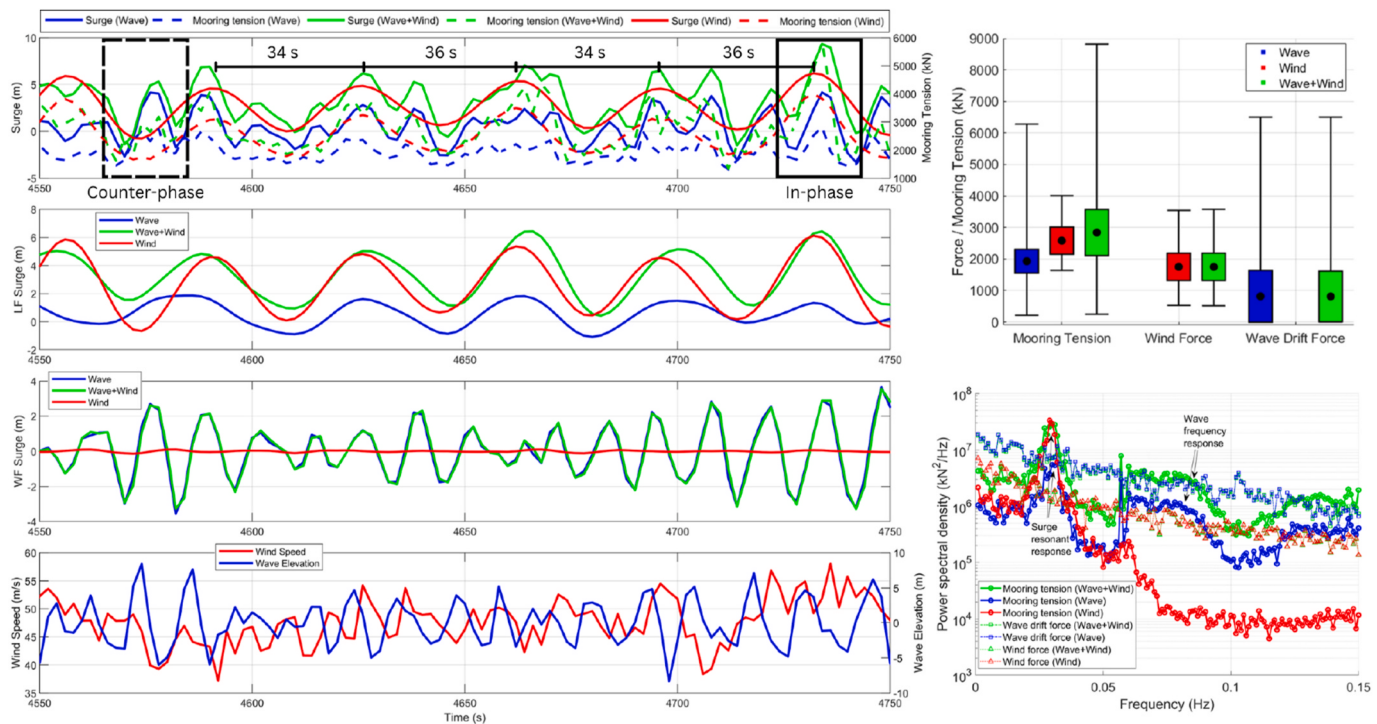


**Fig. 13.** Left: Timeseries of mooring tension, surge; LF surge and WF surge under wind only, wave only and wave with wind conditions; wind speed and wave elevation. Right: Statistical values and PSD chart.

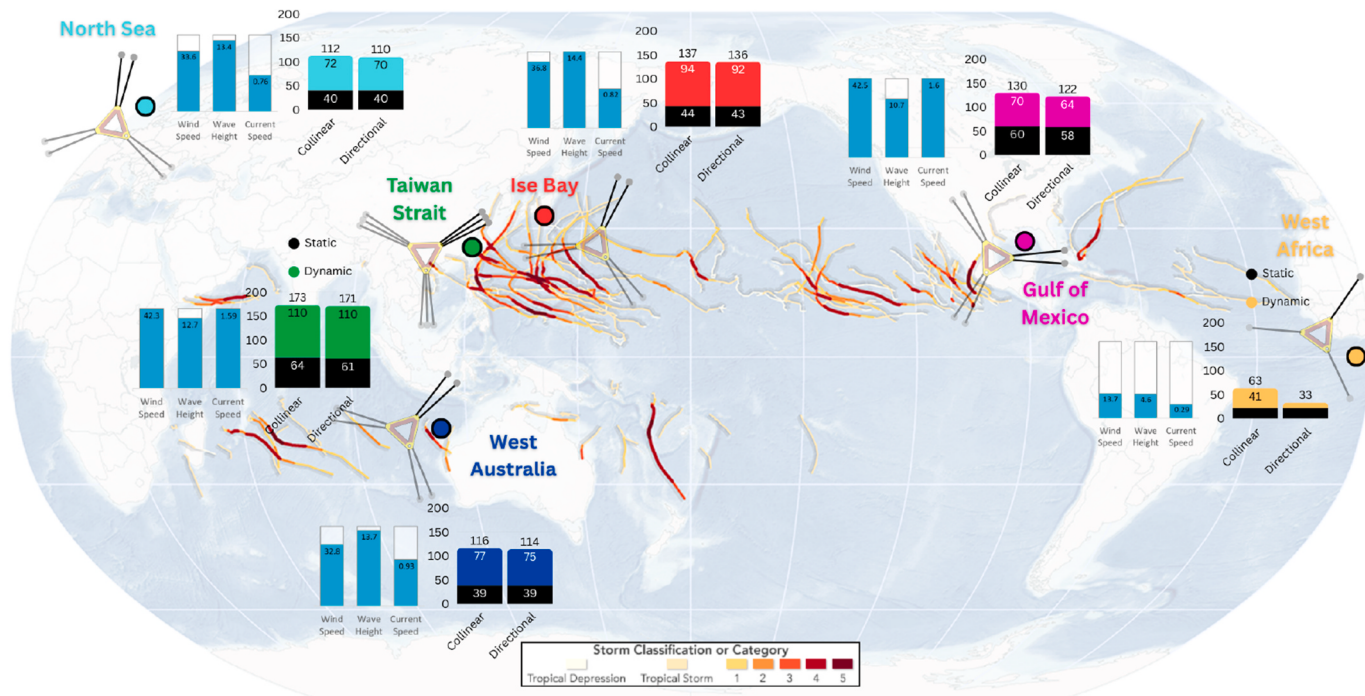


**Fig. 14.** Mooring patterns (220 mm chain), tensions (% of “global” average of all 6 sites) and environmental conditions around the world, overlaid on top of the year 2015’s typhoons map (Stevens et al., 2015) (year with record number of cyclones).

and Gulf of Mexico have the largest total steady-state force, which may partly explain the severe damages that could be incurred historically by typhoons and hurricanes, respectively.

Two environmental load direction principles were analysed: (i) collinear wave, wind and current and (ii) directional with rotated wind ( $15^\circ$ ) and current ( $30^\circ$ ) loads as per API recommendation (API, 2005)

based on Ekman spiral. The collinear condition resulted in higher tension in all six environments. The difference may be small but can be extreme for environments of lower wave height (e.g., West Africa, Gulf of Mexico), allowing material savings if a non-collinear approach is adopted. Load directions from  $0^\circ$  to  $180^\circ$  were analysed. For the specific off-column floater and spread mooring pattern used in this paper, in all

**Table 6**

A required number of mooring lines to withstand the maximum load condition. Chain diameter after deducting 25 25-year corrosion margin. Green indicates the most favourable mooring system, orange – least favourable. All the simulations were done for 3x3 system, if the tension is far below MBL, 1 or 2 lines in one cluster can be removed and their tension added to the remaining line (considering appropriate safety factor).

Chain diameter	North Sea	West Africa	Gulf of Mexico	West Australia	Japan Ise Bay	Taiwan Strait
<b>165 mm</b> (oil & gas industry)	3x2 = 6	3x1 = 3	3x2 = 6	3x3 = 9	3x3 = 9	3x3 = 9
<b>210 mm</b> (vendor catalogue)	3x2 = 6	3x1 = 3	3x2 = 6	3x2 = 6	3x2 = 6	3x3 = 9

environments, the maximum tension direction is 150° for both collinear and directional. Thus, the critical direction is decided by the designs of the mooring and floater, not the environment. This finding might provide an opportunity for future analyses to save computational effort by focusing on the critical directions only. The above tension results were checked for validity by detailed examination of the underlying physics in the Discussion section. Several mechanisms of wind-wave-current interaction are explained and documented.

Noteworthy, the region with the highest mooring tension, surge and yaw (Taiwan Strait) does not coincide with the highest tower bending moment, pitch and heave region (Japan Ise Bay). It can be said that extreme wind speed is the major design constraint for the mooring system, while wave height is the major design constraint for the floater structure and its connection to the turbine tower.

An interesting finding is that wind-wave coupling is the main reason for tension spikes, which happen when low-frequency wind motion, wave drift motion and higher-frequency 1st order wave motion phases align. Another finding is that wave-current interactions are captured through wave drift damping Current force (even though originating from a uniform flow) is dynamically coupled with platform motions and excited at the surge natural frequency, leading to a tension spike. Note that current data is not as readily available as wind data and is sometimes ignored in initial mooring designs in the literature. It shall be emphasised that this research shows that the current force cannot be neglected in any environment.

The results suggest that a better description of the extreme condition is needed, considering the dependency of multivariate and time series, can have a critical impact on reducing extreme tension. Recent work on extreme analysis methodologies targeted toward extreme analysis with multiple variables (Sando et al., 2024), such as wave height, wind speed, and wave period, together with time sequence dependency structure, and its application to tropical cyclones seems critical. The interactions might be partially mitigated by careful tuning of the system's natural frequencies, which includes adjustments to both the floater and the mooring. This research direction has the potential to reduce the mooring tension, and thus the size and cost of the mooring system.

Limitation of this research is outlined here. First, the paper is meant for pre-FEED research, with the focus to discuss the impacts of tropical cyclones to mooring designs. Next, the findings are applicable only to semi-submersible FOWTs equipped with catenary mooring systems. Different types of floating platforms and mooring configurations may lead to different results and interpretations. However, we also emphasize that the concept we study is one of the most promising concepts and the findings are non-trivial.

#### CRediT authorship contribution statement

**Glib Ivanov:** Writing – review & editing, Writing – original draft, Visualization, Validation, Software, Methodology, Investigation, Formal analysis, Data curation. **Phuc-Manh-Dat Dang:** Writing – original draft, Visualization, Validation, Software, Methodology, Investigation, Formal

analysis. **Wei-Ling Tsai:** Writing – original draft, Visualization, Investigation, Formal analysis. **Yuefan Du:** Writing – original draft, Methodology, Investigation, Data curation. **Ryota Wada:** Writing – review & editing, Writing – original draft, Validation, Supervision, Project administration, Methodology, Investigation, Funding acquisition, Formal analysis, Data curation, Conceptualization. **Kai-Tung Ma:** Writing – review & editing, Validation, Supervision, Resources, Project administration, Funding acquisition, Conceptualization.

#### Declaration of competing interest

The authors declare the following financial interests/personal relationships which may be considered as potential competing interests: Ryota Wada reports financial support was provided by Japan Society for the Promotion of Science. Kaitung Ma reports financial support was provided by National Science & Technology Council of Taiwan. If there are other authors, they declare that they have no known competing financial interests or personal relationships that could have appeared to influence the work reported in this paper.

#### Acknowledgements

The authors highly appreciate the funding support from National Science & Technology Council of Taiwan; Grant number 113-2218-E-002 -024. This work was also supported by JSPS KAKENHI Grant Number 24K01090.

#### References

- Abs, 2020. Guide for building and classing floating offshore wind turbine installations. In: The American Bureau of Shipping, Houston (TX), USA. Available from: [https://www.eagle.org/content/dam/eagle/rules-and-guides/current/offshore/195\\_fowt\\_i/fowt-guide-july20.pdf](https://www.eagle.org/content/dam/eagle/rules-and-guides/current/offshore/195_fowt_i/fowt-guide-july20.pdf).
- Aichi Prefecture Coastal Protection Basic Plan Review Committee, 2023. Mater. 2nd Techn. Subcomm. Meet. Available from: <https://www.pref.aichi.jp/uploaded/attachment/478801.pdf>.
- API, 2005. Recommended Practice for Design and Analysis of Stationkeeping Systems for Floating Structures. American Petroleum Institute. Available from. [https://www.api.org/~media/files/news/hurricane/2sk\\_add.pdf](https://www.api.org/~media/files/news/hurricane/2sk_add.pdf).
- Aranha, J.A.P., 1994. A formula for 'wave damping' in the drift of a floating body. J. Fluid Mech. 275, 147–155. <https://doi.org/10.1017/S0022112094002314>.
- Barlrop, N., 1998. Floating Structures: a Guide for Design and Analysis.
- Bloemendaal, N., et al., 2020a. Generation of a global synthetic tropical cyclone hazard dataset using STORM. Sci. Data 7 (1), 40. <https://doi.org/10.1038/s41597-020-0381-2>.
- Bloemendaal, N., et al., 2020b. Estimation of global tropical cyclone wind speed probabilities using the STORM dataset. Sci. Data 7 (1), 377. <https://doi.org/10.1038/s41598-024-54691-9>.
- Central Weather Administration ROC (Taiwan) Ministry of Transport, 2024. National ocean database and sharing system. <https://nodass.namr.gov.tw/gis/#/method/Observation/station/cwa>.
- Chen, C.-A., et al., 2023. Design of mooring system for a 15mw semi-submersible, taidafloat, in Taiwan strait. In: 42nd International Conference on Ocean, Offshore and Arctic Engineering. ASME, Melbourne, Australia.
- Chen, J., et al., 2024. Parametric sensitivity analysis of mooring chains of a floating offshore wind turbine in shallow water. J. Mar. Sci. Eng. 12 (12), 2202. <https://www.mdpi.com/2077-1312/12/12/2202>.

- Cummins, W., 1962. The impulse response functions and ship motion. Schiffstechnik 9, 101–109. <https://scispace.com/pdf/the-impulse-response-function-and-ship-motion-52qh6etk.pdf>.
- Det Norske Veritas, 2024. DNV-ST-0437 Loads and Site Conditions for Wind Turbines.
- Driscoll, F., Lueck, R., Nahon, M., 2000. Development and validation of a lumped-mass dynamics model of a deep-sea ROV system. *Appl. Ocean Res.* 22 (3), 169–182.
- European Committee for Standardization CEN, 2004. Eurocode 1: actions on structures—General actions—Part 1-4: wind actions. <https://www.phd.eng.br/wp-content/uploads/2015/12/en.1991.1.1.2002.pdf>.
- Gaertner, E., et al., 2020. IEA Wind TCP Task 37: Definition of the IEA 15-megawatt Offshore Reference Wind Turbine. National Renewable Energy Lab.(NREL), Golden, CO (United States).
- Grossmann-Matheson, G., et al., 2024. Global tropical cyclone extreme wave height climatology. *Sci. Rep.* 14 (1), 4167. <https://doi.org/10.1038/s41598-024-54691-9>.
- Haddara, M., Soares, C.G., 1999. Wind loads on marine structures. *Mar. Struct.* 12 (3), 199–209. [https://doi.org/10.1016/S0951-8339\(99\)00023-4](https://doi.org/10.1016/S0951-8339(99)00023-4).
- Haocheng, Xue, et al., 2025. Experimental analysis of the movement response of beating frequency waves to semi-submersible floating platform. In: Taiwan SNAME 2025. Taipei, Taiwan.
- Hasselmann, D.E., Dunckel, M., Ewing, J., 1980. Directional wave spectra observed during JONSWAP 1973. *J. Phys. Oceanogr.* 10 (8), 1264–1280.
- Hopstad, A.L.H., et al., 2018. DNV GL standard for floating wind turbines. In: International Conference on Offshore Mechanics and Arctic Engineering. American Society of Mechanical Engineers.
- Hsu, S.A., 2015. Estimating wave height using wind speed during a tropical cyclone. *Mar. weather Log.* 59. <https://www.vos.noaa.gov/MWL/201512/waveheight.shtml>.
- Hsu, I.-J., et al., 2022. Optimization of semi-submersible hull design for floating offshore wind turbines. In: 41st International Conference on Offshore Mechanics and Arctic Engineering (OMAE 2022). American Society of Mechanical Engineers, Hamburg, Germany. <https://doi.org/10.1115/OMAE2022-86751>.
- Huang, W.-H., Yang, R.-Y., 2021. Water depth variation influence on the mooring line design for FOWT within shallow water region. *J. Mar. Sci. Eng.* 9 (4), 409. <https://www.mdpi.com/2077-1312/9/4/409>.
- International Electrotechnical Commission, 2025. Wind Energy Generation Systems - Part 3-2: Design Requirements for Floating Offshore Wind Turbines.
- Ivanov, G., Hsu, I.-J., Ma, K.-T., 2023. Design considerations on semi-submersible columns, bracings and pontoons for floating wind. *J. Mar. Sci. Eng.* 11 (9), 1663. <https://doi.org/10.3390/jmse11091663>.
- Ivanov, G., et al., 2024a. Optimal mooring pattern for a semi-submersible FOWT in a typhoon environment. In: 43rd International Conference on Ocean, Offshore and Arctic Engineering (OMAE2024). ASME, Singapore.
- Ivanov, G., Hsu, I.J., Ma, K.T., 2024b. Overview of FOWT demo projects cost and analyses of hull design features. In: Proceedings of the Third World Conference on Floating Solutions. Springer Nature Singapore, Singapore. [https://doi.org/10.1007/978-981-97-0495-8\\_44](https://doi.org/10.1007/978-981-97-0495-8_44).
- Ivanov, G., Wu, Y., Ma, K.-T., 2025. Optimized mooring solutions for floating offshore wind turbines in harsh environments. *Ocean Eng.* 340, 122289. <https://doi.org/10.1016/j.oceaneng.2025.122289>.
- Jonathan, P., Evans, K., 2013. Statistical modelling of extreme ocean environments for marine design: a review. *Ocean Eng.* 62, 91–109. <https://doi.org/10.1016/j.oceaneng.2013.01.004>.
- Koohi Kheili, A.G., et al., 2022. Characterization of tropical cyclones to identify the response based design metocean conditions for an FPSO mooring system. *Ocean Eng.* 247, 110753. <https://doi.org/10.1016/j.oceaneng.2022.110753>.
- Lee, C., Newman, J., 2005. Computation of wave effects using the panel method. *Numeric. Mod. Fluid Struct. Interact.* 42, 211–251. <https://doi.org/10.2495/978-1-85312-837-0/06>.
- Lee, J., Zhao, F., 2021. GWEC Global Wind Report 2021, 15. Global wind energy council, p. 16. <https://www.gwec.net/reports>.
- Lee, C.-I., Chen, T.-L., Lin, T.-Y., 2024. Experiment on hydrodynamic characteristics of A semi-submersible floating platform. In: 1st Asia Pacific Conference on Offshore Wind Technology (APCOW 2024). Fukuoka, Japan.
- Leong, D., Low, Y.M., Kim, Y., 2018. Long-term extreme response prediction of mooring lines using subset simulation. In: ASME 2018 37th International Conference on Ocean, Offshore and Arctic Engineering. <https://doi.org/10.1115/omae2018-77064>.
- Li, L., Gao, Z., Moan, T., 2015. Joint distribution of environmental condition at five European offshore sites for design of combined wind and wave energy devices. *J. Offshore Mech. Arctic Eng.* 137 (3). <https://doi.org/10.1115/1.4029842>.
- Li, J., et al., 2024. Study on the mooring systems attaching clump weights and heavy chains for improving the typhoon resistance of floating offshore wind turbines. *Ocean Eng.* 311, 118734. <https://doi.org/10.1016/j.oceaneng.2024.118734>.
- Ma, K.-t., et al., 2013. A historical review on integrity issues of permanent mooring systems. In: Offshore Technology Conference. OnePetro.
- Ma, K.-T., et al., 2019. Mooring System Engineering for Offshore Structures. Elsevier. Available from: <https://www.sciencedirect.com/book/9780128185513/mooring-system-engineering-for-offshore-structures>.
- Ma, K.-T., et al., 2025. Wind farm design with 15MW floating offshore wind turbines in typhoon regions. *J. Mar. Sci. Eng.* 13 (4). <https://doi.org/10.3390/jmse13040687>.
- Malenica, Š., Clark, P., Molin, B., 1995. Wave and current forces on a vertical cylinder free to surge and sway. *Appl. Ocean Res.* 17 (2), 79–90.
- Moriarty, P.J., Hansen, A.C., 2005. Aerodyn Theory Manual. National Renewable Energy Lab, Golden, CO (US). Available from: <https://docs.nrel.gov/docs/fy05osti/36881.pdf>.
- Norske Veritas, Det, 2025. DNV-RP-C205 Environmental Conditions and Environmental Loads.
- Organisation, I.S., 2015. Petroleum and Natural Gas Industries — Specific Requirements for Offshore Structures. Part 1: Metocean Design and Operating Considerations.
- Raillard, N., Prevosto, M., Pineau, H., 2019. 3-D environmental extreme value models for the tension in a mooring line of a semi-submersible. *Ocean Eng.* 184, 23–31. <https://doi.org/10.1016/j.oceaneng.2019.05.016>.
- Rui Wen, S., 2020. Fukushima energy failed? Japan announces dismantling of floating turbines. Environ. Inform. Center cited; Available from: <https://e-info.org.tw/node/228593>.
- Sando, K., et al., 2024. Multivariate spatial and spatio-temporal models for extreme tropical cyclone seas. *Ocean Eng.* 309, 118365. <https://doi.org/10.1016/j.oceaneng.2024.118365>.
- Sheng, C., Hong, H.P., 2020. On the joint tropical cyclone wind and wave hazard. *Struct. Saf.* 84, 101917. <https://doi.org/10.1016/j.strusafe.2019.101917>.
- Stanisic, D., et al., 2017. Evaluation of Conventional Methods of Establishing Extreme Mooring Design Loads, V03AT02A017.
- Stanisic, D., et al., 2018. Design loads and long term distribution of mooring line response of a large weathervaning vessel in a tropical cyclone environment. *Mar. Struct.* 61, 361–380. <https://doi.org/10.1016/j.marstruc.2018.06.004>.
- Stevens, J., Carlowicz, M., 2015. Records fall in 2015 cyclone season. NASA Earth Observatory. Available from: <https://earthobservatory.nasa.gov/images/87092/records-fall-in-2015-cyclone-season>.
- Wada, R., Waseda, T., Jonathan, P., 2016. Extreme value estimation using the likelihood-weighted method. *Ocean Eng.* 124, 241–251. <https://doi.org/10.1016/j.oceaneng.2016.07.063>.
- Wada, R., Waseda, T., Jonathan, P., 2018. A simple spatial model for extreme tropical cyclone seas. *Ocean Eng.* 169, 315–325. <https://doi.org/10.1016/j.oceaneng.2018.09.036>.
- Wada, R., et al., 2025. Floating offshore wind in Japan: addressing the challenges, efforts, and research gaps. *Wind Energ. Sci. Discuss.* 1–58. <https://doi.org/10.5194/wes-2025-74>.
- Wang, J., Luo, Y., Lu, R., 2002. Truss spar structural design for West Africa environment. In: International Conference on Offshore Mechanics and Arctic Engineering. <https://doi.org/10.1115/OMAE2002-28245>.
- Wen, Y., Banon, H., 1991. Development of environmental combination design criteria for fixed platforms in the Gulf of Mexico. In: Offshore Technology Conference. OTC. Available from: <https://doi.org/10.4043/6540-MS>.
- World Meteorological Organization, 2017. Global guide to tropical cyclone forecasting. <https://cyclone.wmo.int/pdf/Global-Guide-to-Tropical-Cyclone-Forecasting.pdf>.
- Wu, K.-Y., et al., 2023. Technology development of a floating offshore wind turbine, "TaidaFloat". In: Taiwan Wind Energy Conference 2023. Taiwan Wind Energy Association, Taipei, Taiwan.
- Xia, J., Taghipour, R., 2012. Feasibility of TLP with tender assisted drilling for northwest Australian waters-A case study. In: Offshore Technology Conference. OTC. <https://doi.org/10.4043/23247-MS>.
- Xu, S., Ji, C.-y., Guedes Soares, C., 2021. Short-term extreme mooring tension and uncertainty analysis by a modified ACER method with adaptive Markov Chain Monte Carlo simulations. *Ocean Eng.* 236, 109445. <https://doi.org/10.1016/j.oceaneng.2021.109445>.
- Xu, H., et al., 2024. Dynamic response of floating offshore wind turbine under different stages of typhoon passage. *Appl. Ocean Res.* 148, 104047. <https://doi.org/10.1016/j.apor.2024.104047>.
- Zou, T., et al., 2022. The impact of initial imperfections on the fatigue assessment of tower flange connections in floating wind turbines: a review. *Front. Mar. Sci.* 9. <https://doi.org/10.3389/fmars.2022.1063120>.